ACS APPLIED BIO MATERIALS

www.acsabm.org Article

A Photoelectrochemical Platform Based on Polyaniline-Modified Titanium Dioxide Facet Heterostructure

Yuanyuan Wang, Li Yin, Jie Wu, Nan Li, Na He, Haixin Zhao, Xiaotian Li,* Xiaoyong Lai,* and Qiang Wu*

Cite This: *ACS Appl. Bio Mater.* 2022, 5, 1297−1304 Read Online

ACCESS | Metrics & More | Article Recommendations | Supporting Information

ABSTRACT: A photoelectrochemical (PEC) electrode for glucose detection was built based on polyaniline (PANI) modified titanium dioxide heterojunction (FH-TiO_2) structures. Ultrathin titanium dioxide (TiO_2) nanosheets are assembled onto rutile nanorods (TiO_2 NRs). Experiments show that the main exposed faces of these nanosheets are (101) or (111) crystal planes. Proven by theoretical calculation, the bottom of the conduction band (CB) of (111) is 0.15 eV lower than the bottom of the conduction band of (101). Therefore, when the material is excited by light, photogenerated electrons are able to transfer from the conduction band of (101) to the conduction band of (111). PANI was introduced as a medium to effectively conduct photogenerated charges between glucose oxidase and titanium dioxide. A photoelectric detection electrode for glucose was fabricated by loading glucose oxidase onto PANI@FH-TiO_2. This electrode showed excellent performance in 0.2−1.0 mM linear range with a sensitivity 15.63 μA mM^{-1} cm^{-2} and 1.0−15.0 mM linear range with a sensitivity of 1.42 μA mM^{-1} cm^{-2}.

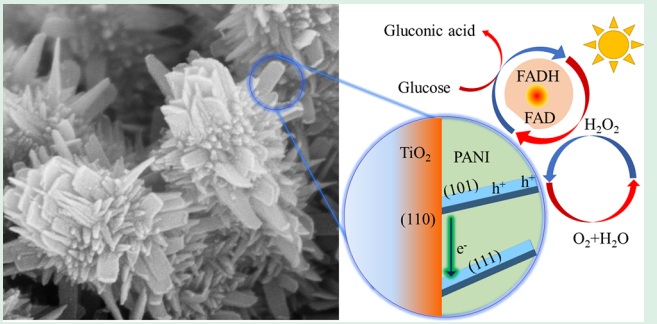

KEYWORDS: *titanium dioxide, facet heterostructure, density functional theory (DFT), polyaniline, photoelectrochemical biosensor*

1. INTRODUCTION

Sensitive and rapid detection of glucose has always played an important role in food, health, and industry.[1−4] Over the past decades, photoelectrochemical (PEC) biosensors have been widely studied as a burgeoning analytical tool for the detection of nucleic acids and other markers.[5−7] Because of the use of photoexcitation and electrical analysis modes, photoelectrochemical analysis can effectively avoid the disadvantage that the input signal and output signal are homologous in electrochemical analysis.[8,9] It is inherently characterized by high signal-to-noise ratio, low detection limit, and easy miniaturization compared with the traditional techniques.[10,11] It is worth mentioning that the photoelectric conversion material is a very important part in the PEC biosensing because it not only acts as a transducer but also acts as a catalyst.[12−14] As a more mature electrochemical system of research, it may be used as a means to explore the relationship between photoelectrochemical performance and sensitive materials. Therefore, the study of photoelectrochemical sensing of glucose has also become the focus of researchers.[15,16]

Among so many photoelectric materials, titanium dioxide is extensively studied for photoelectric biosensing materials because of its efficient photocatalytic ability and environmental benignity.[17−19] The main crystal forms of titanium dioxide are rutile and anatase. Compared with anatase TiO_2, rutile TiO_2 is supposed to be a better photoelectric material.[20,21] Rutile TiO_2 is thermodynamically more stable and has better separation ability of photogenerated electron−holes due to its fewer defects in the crystal. Furthermore, the narrower band gap enables rutile TiO_2 to expand the absorption-band edge from ∼380 nm (for anatase TiO_2) to ∼400 nm.[22] However, rutile TiO_2 is usually at a disadvantage in the competition with anatase TiO_2 due to its higher carrier recombination rate. Therefore, reducing carrier recombination rate has become an important issue for the application of rutile TiO_2 in PEC biosensing.[23−25] Inspired by "surface heterojunction", Liu's group[26] introduced a facet-heterojunction (FH) strategy. Studies have shown that this method can effectively inhibit the recombination of photogenerated electron−hole pairs. Generally speaking, a high-quality interface can improve the space-time separation efficiency of carriers. Unfortunately, most of the inorganic−inorganic composite materials are prepared by physical mixing or gradual deposition methods,[27,28] resulting in material interfaces that need to be further optimized. Introducing a carrier conduction medium between

Received: December 24, 2021
Accepted: February 28, 2022
Published: March 9, 2022

https://doi.org/10.1021/acsabm.1c01298
ACS Appl. Bio Mater. 2022, 5, 1297−1304

Scheme 1. (a) PANI@FH-TiO_2 Electrode Construction, (b) Theoretical Calculations of (111) and (101) Exposed Nanosheet, (c) Detection Principle of the PANI@FH-TiO_2 Electrode

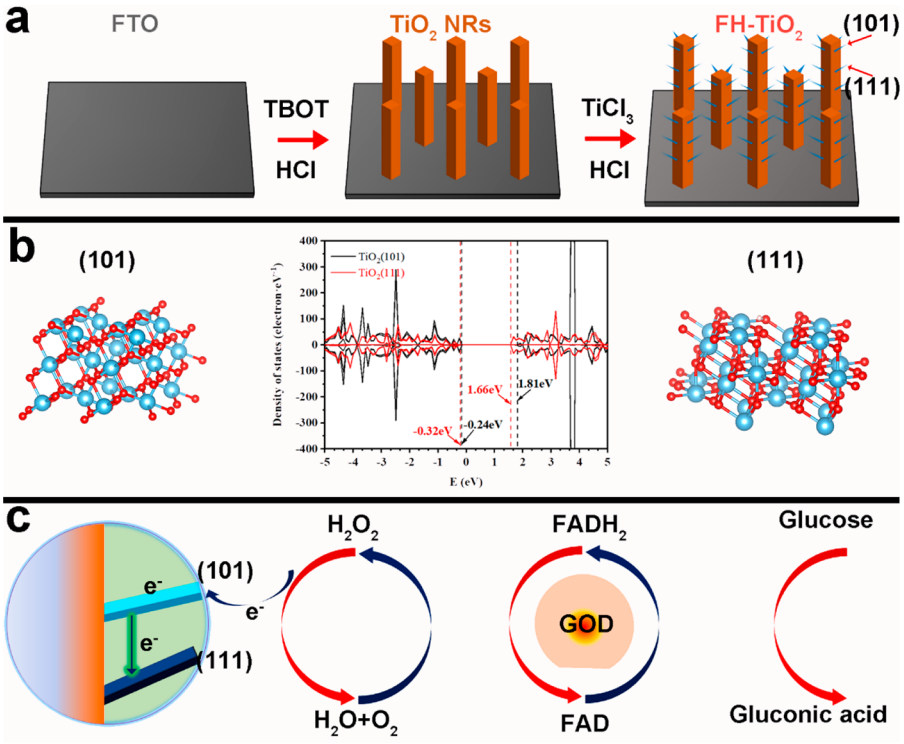

FHs should be an effective solution to settle the matter of charge recombination caused by carrier propagation between crystal interfaces. Polyaniline has become an excellent candidate for electronic media due to its easy preparation, reversible redox, environmental friendliness, and controllable conductivity.[29−31] In fact, it has been widely used in constructing PEC sensors. For example, Ju and co-workers[32] applied polyaniline (PANI)/titanium dioxide (TiO_2) nanotube composite to lactic acid photoelectric detection and obtained higher photocatalytic activity. Similarly, the previous research of our group has also shown that the addition of PANI effectively inhibits the recombination of photogenerated charges.[33]

Herein, a photoelectrochemical platform was built based on polyaniline modified titanium dioxide facet heterojunction (FH-TiO_2) structures, and polyaniline was introduced into the FH structure as an electronic medium. Synthesis procedure and detection principle of the PANI@FH-TiO_2 electrode are presented in Scheme 1a. First, TiO_2 nanorods (NRs) were grown on FTO by a simple hydrothermal process. Titanium dioxide nanosheets were then assembled on rutile NRs via a sequential hydrothermal synthesis. After electrodepositing PANI onto FH-TiO_2 nanoarrays, a PEC-biosensing platform was successfully fabricated by loading glucose oxidase on the PANI@FH-TiO_2 electrode. The theoretical calculation was applied to obtain the states density of (111) and (101) of titanium dioxide facet. The rutile TiO_2 nanosheets calculation model was built by cutting TiO_2 crystals. A 20 Å vacuum region was subjoined along the perpendicular direction to the section of the TiO_2 crystals. Two-dimensional periodic boundary condition was set along the parallel direction of the sections.[26] From Scheme 1b, both of the exposed sections were dominated by O atoms. There are more five-coordinated titanium atomic dangling bonds on the (111) than on the (101). From the electronic density of states (DOS) of two TiO_2 nanosheets, the conduction-band minimum of the (111) was 0.15 eV lower in energy than the conduction-band minimum of the (101). Thereby, the photogenerated electrons in the (101) exposed nanosheet would directionally move into (111) exposed nanosheet along the PANI wire. In brief, the band alignment in the facet heterojunction could facilitate directional movement of electron and inhibit electron−hole recombination. The detection principle of the sensor is provided in Scheme 1c. When glucose was oxidized to gluconic acid by glucose oxidase, O_2 was reduced to H_2O_2 simultaneously. The photogenerated holes gathered on the (101) crystal plane and were consumed by H_2O_2 to form an electric current. The chemical equations of the detection principle were presented in the Supporting Information page S1.

2. EXPERIMENTAL SECTION

2.1. Materials and Reagents. F-doped tin oxide (FTO; 1 cm × 2 cm) glasses were bought from Hefei Kojing Material Technology Co., Ltd. Hydrochloric acid (HCl), tetrabutyl titanate (TBOT), titanium trichloride ($TiCl_3$), ethyl alcohol (CH_3CH_2OH), sodium chloride (NaCl), ascorbic acid (AA), urea (UA), fructose (Fru), and glucose (Glu) were acquired from Sinopharm Chemical Reagent Guangzhou Co., Ltd. Glucose oxidase (GOD), glutathione (GSH), and dopamine (DA) were purchased from Shanghai Aladdin Bio-Chem Technology Co., Ltd. Glass cleaner was acquired from Shenzhen Run Ming Tong Technology Co., Ltd.

2.2. Apparatus. The morphology of simples was acquired by scanning electron microscopy (Hitachi SU8010). Crystal structure information of the materials was obtained on a transmission electron microscope (Nippon Electronics Co., Ltd. JEM 2100). X-ray diffraction (XRD) was acquired from a powder diffractometer (Rigaku, Smart Lab). Diffuse reflectance spectrum was tested on UV−vis absorption spectrophotometer (Thermo Fisher Evolution

https://doi.org/10.1021/acsabm.1c01298
ACS Appl. Bio Mater. 2022, 5, 1297−1304

220). Fourier transform infrared spectra (FTIR) were obtained from a Fourier transform infrared spectrometer (BRUKER, T27). Raman spectra were characterized from Raman spectrograph (Renishaw plc Company, in Via). X-ray photoelectron spectroscopy (XPS) was tested by a X-ray photoelectron spectrometer (Thermo Scientific, ESCALAB250).

2.3. Synthesis of TiO_2 Nanorod Arrays (NRs). Ten milliliters of deionized water was mixed with equal amounts of HCl (37%). After dropwise addition of 400 μL of TBOT, this mixture was stirred for 30 min until the solution was homogeneous and transparent. The mixture was transferred into an autoclave. After being ultrasonically cleaned in glass cleaner, the FTO glass was placed in the autoclave with the conductive surface facing down. The autoclave was set to 150 °C for 4 h. Afterward, the substrates were taken out and washed with deionized water to wait for the next step.

2.4. Synthesis of FH-TiO_2 Electrodes. FH-TiO_2 electrodes were synthesized via a sequential hydrothermal synthesis. Then 0.25 mL of $TiCl_3$ and 0.25 mL of HCl (37%) were mixed with 20 mL of deionized water in a 50 mL autoclave. After TiO_2 NRs substrates were placed in, the autoclave was heated at 80 °C for 60 min. The FH-TiO_2 electrodes were washed by deionized water and dried in an oven at 50 °C overnight. To increase crystallinity, FH-TiO_2 electrodes were annealed at 450 °C for 3 h in air and dried in an oven at 50 °C overnight.

2.5. Fabrication of GOx-PANI@FH-TiO_2 Electrode. To introduce polyaniline, the FH-TiO_2 electrodes were placing in a 0.1 M aniline solution for 30 min. Constant-potential electrodeposition was carried out under 0.9 V in a diluted sulfuric acid solution (0.5 M) with 0.05 M aniline. To prepare the GOx-PANI@FH-TiO_2 PEC electrode, the electrode was rinsed in ultrapure water, and then 20 μL of GOx (10 mg mL^{-1}) was dispersed on PANI@FH-TiO_2 electrode. After dried in the fridge at 4 °C for 8 h, GOx-PANI@FH-TiO_2 electrode was rinsed with ultrapure water to remove unbound enzymes.

2.6. PEC Performance Tests. PEC performance tests were performed in a quartz photoelectrolytic cell full of PBS (pH 7.0) buffer by electrochemical workstation (Chenhua, CHI 660E). Xenon lamp (Zhongjiaojinyuan, CEL-HXUV 300) was used as excitation signal source. A three-electrode system was established with GOx-PANI@FH-TiO_2 work electrode, Ag/AgCl (3 M KCl) reference electrode, and Pt foil (1 cm × 1 cm) counter electrode. EIS was performed at 100 kHz to 1000 Hz frequency with 5 mV AC perturbation.

3. RESULTS AND DISCUSSION

3.1. Morphology Characterization. Surface morphologies of the TiO_2 NRs, FH-TiO_2, and PANI@FH-TiO_2 electrodes are displayed in Figure 1. Figure 1a and b show top-views of TiO_2 NRs electrode at different magnifications. It can be observed that the diameter of the nanorods was 100 nm and they were tightly arranged. Figure 1c presents top-view images of FH-TiO_2 electrodes, ultrathin TiO_2 nanosheets uniformly assembled on the rutile TiO_2 nanorods. From the high-amplification image in Figure 1d, the intimate and homogeneous combination could secure efficient transfer of electrons between nanosheets and TiO_2 NRs. The top-view images of PANI@FH-TiO_2 are shown in Figure 1e. Additionally, the high-amplification image of the sample in Figure 1f revealed that the organic coating did not completely seal the electrode surface, leaving room for the diffusion of substances and light absorption. The TEM images of PANI@FH-TiO_2 electrode were presented in Figure S1, and the morphology of rutile TiO_2 NRs (Figure S1a) was reproduced the FESEM image with high fidelity. Figure S1b shows that some small nanosheets were close to rutile TiO_2 nanorods, and the clear and regular lattice stripes illustrated the good crystallinity of the material. The crystal-plane spacing of the nanosheets was

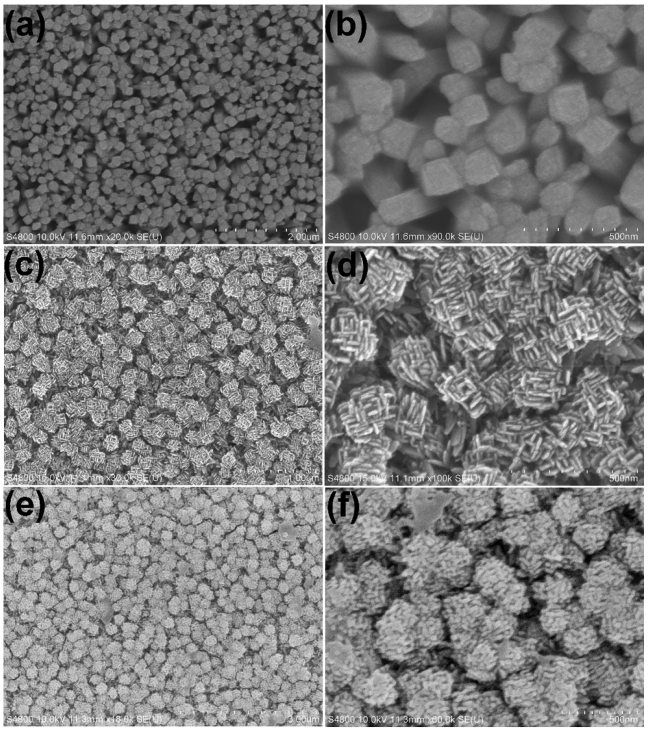

Figure 1. SEM image top view of (a, b) TiO_2 NRs; (c, d) FH-TiO_2 heterostructure; (e, f) PANI@FH-TiO_2 electrodes.

0.22 and 0.25 nm, indicating that the exposed crystal planes were (111) and (101).[26]

3.2. Component Analysis. The crystal structure of TiO_2 NRs, FH-TiO_2 heterostructures, and PANI@FH-TiO_2 composites electrode was further investigated by X-ray diffraction. In Figure 2, the TiO_2 NRs showed peaks located at 23.1°, 51.78°,

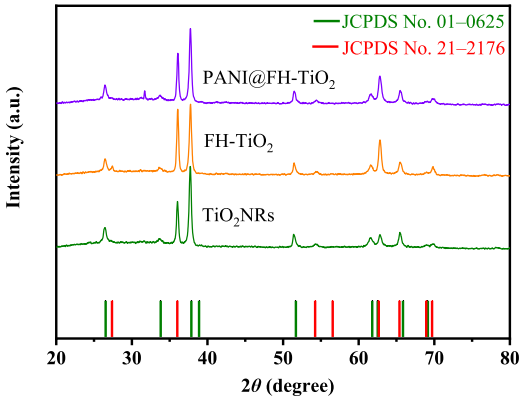

Figure 2. XRD patterns of rutile TiO_2 nanorod array, FH-TiO_2 heterostructures, and PANI@FH-TiO_2 electrode on FTO substrate.

54.8°, 61.9°, and 69.2°, which were consistent with SnO_2. In addition, the diffraction peaks at 36.0°, 54.3°, 62.7°, 65.5°, 65.8°, 69.0°, and 69.8° were assigned to the rutile TiO_2 NRs, and it was observed that the crystallinity of TiO_2 NRs was good.[22] The same diffraction patterns were found in the FH-TiO_2 electrode, while the characteristic peak intensities at 36.0° and 62.7° increased, indicating that the nanosheets had special exposed crystal planes on (101) and (001).[26] According to the XRD pattern, the characteristic peaks at 15.0°, 21.0°, and 25.6° corresponded to the (010), (100), and

https://doi.org/10.1021/acsabm.1c01298
ACS Appl. Bio Mater. 2022, 5, 1297−1304

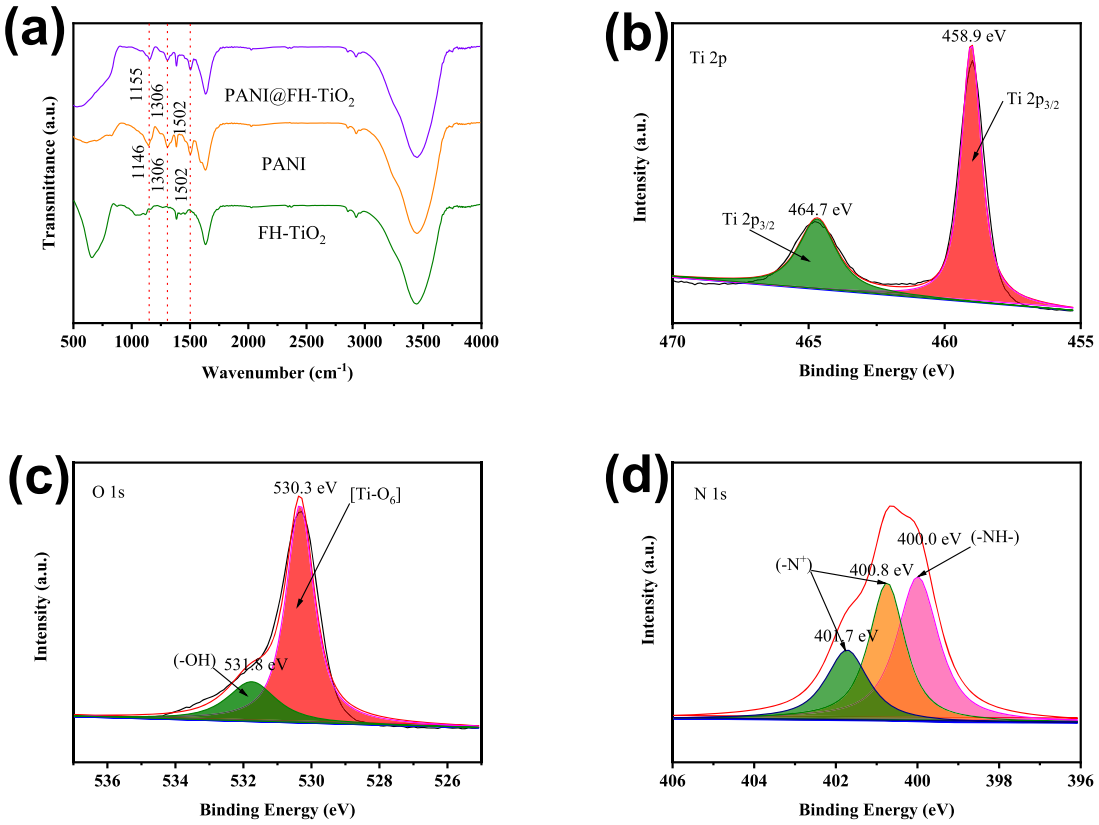

Figure 3. (a) FTIR spectrum of rutile TiO_2, FH-TiO_2, and PANI@FH-TiO_2; high-resolution XPS analysis of PANI@FH-TiO_2 electrode (b) Ti 2p, (c) O 1s, and (d) N 1s.

(110) of PANI, indicating that this organic layer was emeraldine salt PANI.[32]

The component information of TiO_2 NRs, FH-TiO_2 heterostructures, and PANI@FH-TiO_2 composites electrode was further investigated through FTIR spectrometry (Figure 3a). Infrared spectroscopy has its unique advantages when characterizing organic matter, so we used it to characterize the bonding situation of PANI on the material. The FTIR spectrum of FH-TiO_2 showed a broad peak located at 3450 cm^{-1} that was due to stretching vibration of surface hydroxyl. The absorption band between 500 cm^{-1} and 800 cm^{-1} was because of the titanium-oxide chain bridging vibration pattern and stretching pattern.[20] Infrared results of electrodes after polyaniline deposition showed three new characteristic peaks, the C−H in-plane bending vibration of the substituted benzene (1146 cm^{-1}), C=C stretching vibration of quinoid and benzenoid rings (1306 cm^{-1}), and N=P=N (P represents the quinoid ring) stretching (1502 cm^{-1}). After polyaniline is deposited on the electrode, the peak of in-plane vibration of the carbon−hydrogen bond on the benzene ring was shifted from 1146 to 1155 cm^{-1}, which proved that the powerful N−O bond confined the vibration of polyaniline chain.[32]

The XPS spectra of PANI@FH-TiO_2 are shown in Figure 3b−d. There are two characteristic peaks in the Ti 2p spectrum (Figure 3b) corresponding to $2p_{3/2}$ orbit (458.9 eV) and $2p_{1/2}$ orbit (464.7 eV) of titanium, respectively. In Figure 3c, there are two peaks in O 1s orbital spectrum, corresponding to the surface −OH group (530.3 eV) and the O atoms in the TiO_2 lattice (531.8 eV). The 1s orbital spectrum of N (Figure 3d) is composed of one main peak (400.0 eV) and two accompanying peaks (400.8 and 401.7 eV). The main peak is related to the amino group (−NH) in polyaniline-H_2SO_4. The two accompanying peaks correspond to the binding energies of the nitrogen atoms in the protonated imines (400.8 eV, $-N^+=$) and amino groups (401.7 eV, $-N^+H-$). According to previous research, the ratio of the sum of the areas of the first two peaks to the area of the peak at 400.9 eV was high, which indicated that the PANI had better conductivity.[20,32]

3.3. PEC Analysis. Figure 4a shows that the electrodes both have a lower dark current indicating a low-noise character and electrodes respond quickly to light. The photocurrent of FH-TiO_2 electrode was ∼25% higher than of TiO_2 NRs electrode because the formation of facet heterojunction improved charge separation efficiency and inhibited the photogenerated carrier recombination. PANI@FH-TiO_2 electrodes showed ∼40% higher photoresponse current than that of TiO_2 NRs electrode. It may be because the introduction of polyaniline establishes a bridge for electron transfer between facet heterojunctions and further improves the efficiency of electron transfer.

Fundamentally, the photoelectrochemical process contains three processes: light absorption, charge separation, and surface reaction. Correspondingly, spectroscopy and electrochemical methods are performed to explore the light absorption capacity, electron−hole separation ability, and surface reaction rate of materials. The light-absorption properties of TiO_2 NRs, FH-TiO_2, and PANI@FH-TiO_2 electrodes were researched by UV−vis diffuse reflectance spectroscopy (Figure S2). From Figure S2a, FH-TiO_2 electrode exhibited high absorption only in the UV range, while the absorption of PANI@FH-TiO_2 electrode raised not only in the ultraviolet region but also in the visible region. The

https://doi.org/10.1021/acsabm.1c01298
ACS Appl. Bio Mater. 2022, 5, 1297−1304

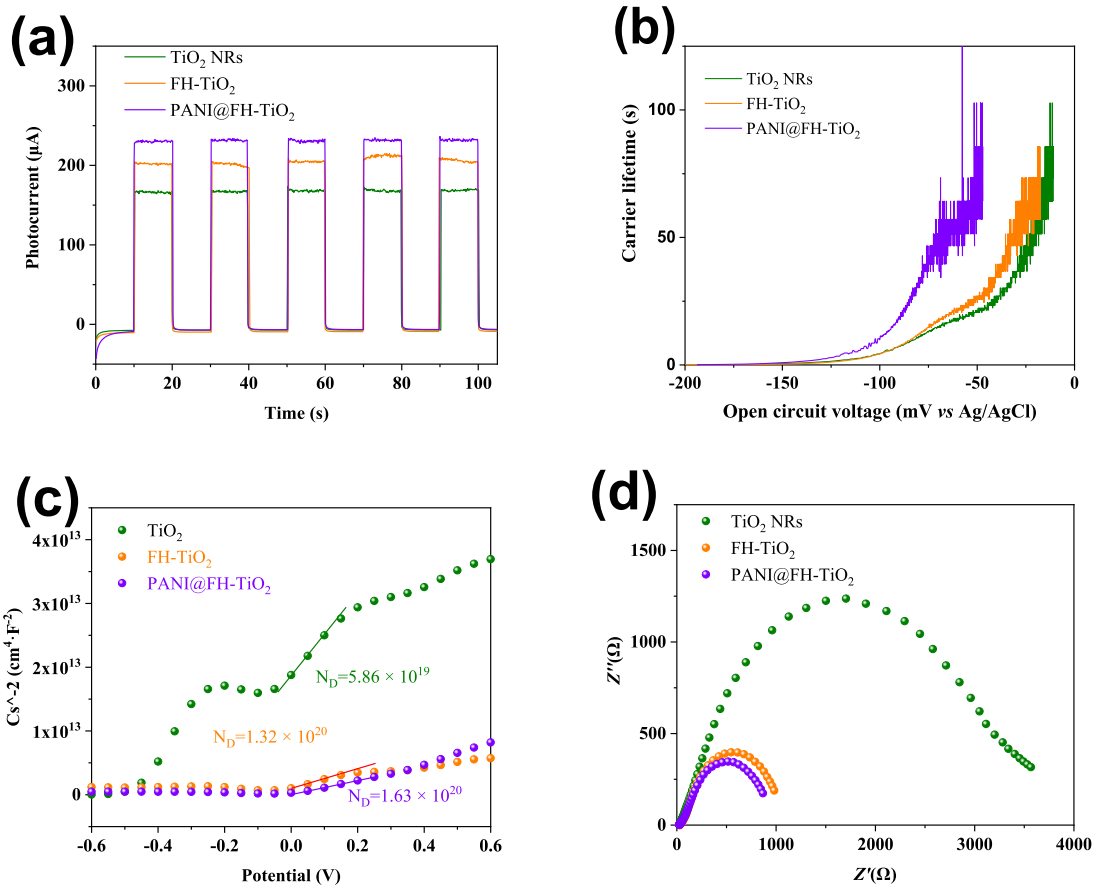

Figure 4. (a) Photocurrent response; (b) OCP plots; (c) Mott−Schottky plots; and (d) EIS Nyquist plots of TiO_2 NRs (green curve), FH-TiO_2 heterostructures (orange curve), and PANI@FH-TiO_2 electrodes (purple curve).

increase in absorption in the 350−400 nm wavelength range was due to excitation of conjugated π electrons of ES-PANI. The increase in 400−800 nm region may be due to configuration change of polyaniline long chain. The bandgap of the material can be calculated from the intercept of the straight line in the plot of $(\alpha h\nu)^{1/2}$ versus $h\nu$. The relationship between $(\alpha h\nu)^{1/2}$ and $h\nu$ is provided in Figure S2b. The band gaps of TiO_2 NRs, FH-TiO_2, and PANI@FH-TiO_2 electrodes were calculated according to eq 1:

$$(\alpha h\nu)^{1/2} = A(h\nu - E_g) \tag{1}$$

The bandgap of FH-TiO_2 electrode was smaller than that of TiO_2 NRs electrode, which may be because of energy-level coupling of the (111) and (101) crystal plane. It is can be seen in the figure that the introduction of polyaniline does not change the band gap.

The open circuit voltage (OPC) attenuation spectra at time after light was turned off were used to reflect the electron lifetime in the material (Figure S2). The electron lifetime of the whole electrode can be reflected by eq 2. A graph of carrier lifetime versus OCP is provided in Figure 4b; compared with TiO_2 NRs electrode and FH-TiO_2, the electron lifetime of PANI@FH-TiO_2 electrode was longer:

$$\tau = \frac{k_B T}{e}\left(\frac{dV_{oc}}{dt}\right)^{-1} \tag{2}$$

The carrier density can be investigated by relationship between surface capacitance and applied voltage. Eq 3 reflects the relationship between surface capacitance and applied voltage:[22]

$$\frac{1}{C^2} = \frac{2}{\varepsilon_0 \varepsilon e N_D}\left[(U_S - U_{FB}) - \frac{k_B T}{e}\right] \tag{3}$$

where C is the space-charge capacitance at the electrode/electrolyte interface, N_D is the electron density, ε_0 is the vacuum permittivity, ε is the dielectric constant of the semiconductor (170 for rutile), and e is the element charge value. Additionally, U_{FB} and U_S are the Femi level and applied potential, k_B is Boltzmann constant, and T is the thermodynamic temperature. The carrier density N_D was calculated on the basis of eq 4:[22]

$$N_D = -\left(\frac{2}{e\varepsilon\varepsilon_0}\right)\left(\frac{d(1/C^2)}{d(U_S)}\right)^{-1} \tag{4}$$

The calculated N_D values for TiO_2 NRs, FH-TiO_2, and PANI@FH-TiO_2 electrodes were 5.86×10^{19}, 1.32×10^{20}, and 1.63×10^{20}, respectively (Figure 4c). It may be because the conjugation structure of PANI molecular chain can catch photogenerated charges, thereby inhibiting charge recombination and increasing the carrier density in the bulk phase.

Charge-transfer capability was characterized by impedance measurements (Figure 4d). TiO_2 NRs, FH-TiO_2, and PANI@FH-TiO_2 electrodes possessed an impedance loop related to charge-transfer processes. The electron-transfer impedance of FH-TiO_2 electrode was smaller than that of TiO_2 NRs

https://doi.org/10.1021/acsabm.1c01298
ACS Appl. Bio Mater. 2022, 5, 1297−1304

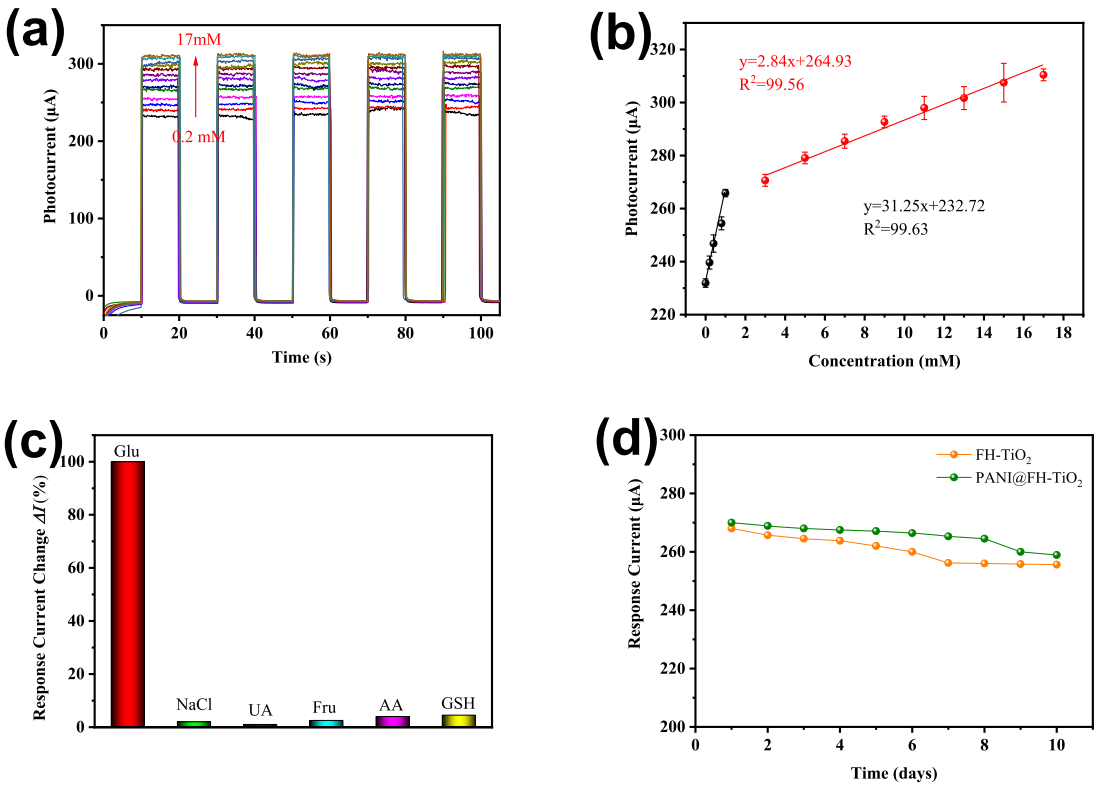

Figure 5. (a) Photocurrent of GOx/PANI@FH-TiO_2 electrode with different concentration of glucose. (b) Calibration curve of different glucose concentration versus photoresponse current. (c) Photocurrent responses change of GOx/PANI@FH-TiO_2 electrodes with amperometric response to 1 mM glucose and different interferences of GOx/PANI@FH-TiO_2 electrodes. (d) Stability of the GOx/PANI@FH-TiO_2 electrode to 1 mM glucose tested in 10 days.

electrode. Once the nanosheets with exposed (111) and (101) crystal planes were connected by rutile nanorods, electrons will transfer from (111) facet to (101) facet. The construction of facet heterojunction formed a self-built electric field, which would provide power for the movement of separated charges. When PANI was deposited onto the heterojunction surface, the PANI@FH-TiO_2 electrode exhibited the smallest slope.

3.4. Glucose-Analysis Performance. To determine the optimum test conditions of the detection system, photoresponse currents of GOx/PANI@FH-TiO_2 electrode to 1 mM glucose were evaluated at different conditions (Figure S3). In Figure S3a, the response current of the electrode rose with increased amount of enzyme. It is since more enzymes can catalyze glucose to produce more H_2O_2. When the amount of enzyme reached 20 mg/mL, further increased enzyme content will cause photocurrent decrease because too many enzymes formed an insulating layer, hindering signal collection. Similarly, Figure S3b shows that when pH reached 7.0, the light-response current of glucose reached its maximum value because the enzyme had the strongest activity within pH 6.5−7.0, and the alkaline environment caused the enzyme's activity to drop rapidly. Time-dependent photocurrent measurements on the GOx/PANI@FH-TiO_2 electrode were tested with 0.2 mM, 0.4 mM, 0.6 mM, 0.8 mM, 1.0 mM, 3.0 mM, 5.0 mM, 7.0 mM, 9.0 mM, 11 mM, 13 mM, 15 mM, and 17 mM glucose. As displayed in Figure 5a, the small fluctuation and short response time of the photoresponse indicate the stability and rapid response characteristics of the detection platform. The sensitivity of GOx/PANI@FH-TiO_2 electrode to glucose is 15.63 μA mM^{-1} cm^{-2} (R^2 = 0.9963) in the 0.2−1.0 mM range and 1.42 μA mM^{-1} cm^{-2} (R^2 = 0.9956) in the 3.0−17 mM range, respectively (Figure 5b). Several kinds of interferences were also evaluated to determine the specificity of GOx/PANI@FH-TiO_2 electrode, and the results are displayed in Figure 5c. Response of GOx/PANI@FH-TiO_2 electrode to other interferences was much smaller than that to glucose. Long-term stability of GOx/PANI@FH-TiO_2 electrode is presented in Figure 5d. When PANI was introduced into the system, the electrode showed good long-term stability. It may be because the suitable microenvironment was constructed near the enzyme and maintaining the enzyme activity in a longer period. The performance comparison table of the detection platform is presented in Table S1.

4. CONCLUSION

A glucose PEC biosensor was reported based on TiO_2 facet heterojunction. PANI was modified on the electrode to build a medium for electron transport between exposed crystal planes and GOx. Theoretical calculations prove that the valence band of the (111) exposed nanosheet is lower than that of (101), which can promote the photogenerated electrons to move in a specific direction, thereby reducing the recombination rate. In addition, when PANI was introduced between facet heterojunctions, the optoelectronic properties of the electrodes have been significantly improved. Subsequent optoelectronic tests showed that polyaniline can not only improve the photocatalytic performance of the entire heterojunction system but also enable more effective interaction between the biologically active part and the optoelectronic material part. GOx/PANI@FH-TiO_2 electrode was applied in glucose PEC detection, achieving good sensitivity, anti-interference, and stability. This

https://doi.org/10.1021/acsabm.1c01298
ACS Appl. Bio Mater. 2022, 5, 1297−1304

work can serve as a reference for the development of safe and fast PEC biosensing devices in the future.

■ ASSOCIATED CONTENT

Supporting Information

Reaction equations, transmission electron microscopy images of FH-TiO_2, UV−vis diffuse reflectance spectrogram, time-open circuit voltage tests, parameters optimization of the PEC biosensor was supplied in Supporting Information. The Supporting Information is available free of charge at https://pubs.acs.org/doi/10.1021/acsabm.1c01298.

(PDF)

■ AUTHOR INFORMATION

Corresponding Authors

Xiaotian Li − *Key Laboratory of Automobile Materials (Jilin University), Ministry of Education, College of Materials Science and Engineering, Jilin University, Changchun 130012, P. R. China;* orcid.org/0000-0002-1513-2300; Phone: +86 431 85168444; Email: xiaotianli@jlu.edu.cn; Fax: +86 431 85168444

Xiaoyong Lai − *Key Laboratory of Energy Resource and Chemical Engineering, State Key Laboratory Cultivation Base of Natural Gas Conversion, School of Chemistry and Chemical Engineering, Ningxia University, Yinchuan 750021, P. R. China;* orcid.org/0000-0002-1273-4111; Phone: +86 951 2061456; Email: xylai@nxu.edu.cn; Fax: +86 951 2061323

Qiang Wu − *Key Laboratory of Tropical Translational Medicine of Ministry of Education, NHC Key Laboratory of Tropical Disease Control, School of Tropical Medicine and The Second Affiliated Hospital, Hainan Medical University, Haikou, Hainan 571199, China;* orcid.org/0000-0003-3922-5189; Phone: +86 898 66984599; Email: wuqiang001001@aliyun.com; Fax: +86 898 66984599

Authors

Yuanyuan Wang − *Key Laboratory of Automobile Materials (Jilin University), Ministry of Education, College of Materials Science and Engineering, Jilin University, Changchun 130012, P. R. China; Key Laboratory of Tropical Translational Medicine of Ministry of Education, NHC Key Laboratory of Tropical Disease Control, School of Tropical Medicine and The Second Affiliated Hospital, Hainan Medical University, Haikou, Hainan 571199, China*

Li Yin − *Key Laboratory of Tropical Translational Medicine of Ministry of Education, NHC Key Laboratory of Tropical Disease Control, School of Tropical Medicine and The Second Affiliated Hospital, Hainan Medical University, Haikou, Hainan 571199, China*

Jie Wu − *Key Laboratory of Tropical Translational Medicine of Ministry of Education, NHC Key Laboratory of Tropical Disease Control, School of Tropical Medicine and The Second Affiliated Hospital, Hainan Medical University, Haikou, Hainan 571199, China*

Nan Li − *Key Laboratory of Automobile Materials (Jilin University), Ministry of Education, College of Materials Science and Engineering, Jilin University, Changchun 130012, P. R. China;* orcid.org/0000-0002-3614-9558

Na He − *Key Laboratory of Tropical Translational Medicine of Ministry of Education, NHC Key Laboratory of Tropical Disease Control, School of Tropical Medicine and The Second Affiliated Hospital, Hainan Medical University, Haikou, Hainan 571199, China*

Haixin Zhao − *Key Laboratory of Automobile Materials (Jilin University), Ministry of Education, College of Materials Science and Engineering, Jilin University, Changchun 130012, P. R. China*

Complete contact information is available at: https://pubs.acs.org/10.1021/acsabm.1c01298

Notes

The authors declare no competing financial interest.

■ ACKNOWLEDGMENTS

This research was financially supported by the National Natural Science Foundation of China (No. 81860373, 21673097, 82060386), the Finance Science and Technology Project of Hainan Province (No. 2019RC221), CAMS Innovation Fund for Medical Sciences (No. 2019-I2M-5-023), Research and Cultivation Fund of Hainan Medical University (No. 19).

■ REFERENCES

(1) Xian, Y.; Hu, Y.; Liu, F.; Xian, Y.; Wang, H.; Jin, L. Glucose biosensor based on Au nanoparticles-conductive polyaniline nanocomposite. *Biosens. Bioelectron.* **2006**, *21* (10), 1996−2000.

(2) Tang, W.; Li, L.; Zeng, X. A glucose biosensor based on the synergistic action of nanometer-sized TiO_2 and polyaniline. *Talanta* **2015**, *131*, 417−23.

(3) Mazeiko, V.; Kausaite-Minkstimiene, A.; Ramanaviciene, A.; Balevicius, Z.; Ramanavicius, A. Gold nanoparticle and conducting polymer-polyaniline-based nanocomposites for glucose biosensor design. *Sens. Actuators, B* **2013**, *189*, 187−193.

(4) Yu, Z.; Li, H.; Zhang, X.; Liu, N.; Tan, W.; Zhang, X.; Zhang, L. Facile synthesis of $NiCo_2O_4$@Polyaniline core-shell nanocomposite for sensitive determination of glucose. *Biosens. Bioelectron.* **2016**, *75*, 161−5.

(5) Huang, L.; Zhang, L.; Yang, L.; Yuan, R.; Yuan, Y. Manganese porphyrin decorated on DNA networks as quencher and mimicking enzyme for construction of ultrasensitive photoelectrochemistry aptasensor. *Biosens. Bioelectron.* **2018**, *104*, 21−26.

(6) Dong, Y. X.; Cao, J. T.; Liu, Y. M.; Ma, S. H. A novel immunosensing platform for highly sensitive prostate specific antigen detection based on dual-quenching of photocurrent from CdSe sensitized TiO_2 electrode by gold nanoparticles decorated polydopamine nanospheres. *Biosens. Bioelectron.* **2017**, *91*, 246−252.

(7) Hu, C.-L.; Pan, H.-J.; Ma, R.-N.; Cheng, S.; Jia, L.-P.; Zhang, W.; Shang, L.; Xue, Q.-W.; Wei, Q.; Wang, H.-S., Gold Nanoparticle-Attached Perovskite $Cs_3Bi_2Br_9$ QDs/BiOBr Heterostructures for Photoelectrochemical Biosensing. *ACS Applied Nano Materials* 2022.

(8) Zhang, X.; Liu, Y.; Kang, Z. 3D branched ZnO nanowire arrays decorated with plasmonic au nanoparticles for high-performance photoelectrochemical water splitting. *ACS Appl. Mater. Interfaces* **2014**, *6* (6), 4480−9.

(9) Yan, Z.; Wang, Z.; Miao, Z.; Liu, Y. Dye-Sensitized and Localized Surface Plasmon Resonance Enhanced Visible-Light Photoelectrochemical Biosensors for Highly Sensitive Analysis of Protein Kinase Activity. *Anal. Chem.* **2016**, *88* (1), 922−9.

(10) Pang, X.; Bian, H.; Wang, W.; Liu, C.; Khan, M. S.; Wang, Q.; Qi, J.; Wei, Q.; Du, B. A bio-chemical application of N-GQDs and g-C_3N_4 QDs sensitized TiO_2 nanopillars for the quantitative detection of pcDNA3-HBV. *Biosens. Bioelectron.* **2017**, *91*, 456−464.

(11) Cai, G.; Yu, Z.; Tang, D. Actuating photoelectrochemical sensing sensitivity coupling core-core-shell Fe3O4@C@TiO2 with molecularly imprinted polypyrrole. *Talanta* **2020**, *219*, 121341.

(12) Li, Y.; Zhang, S.; Dai, H.; Hong, Z.; Lin, Y. An enzyme-free photoelectrochemical sensing of concanavalin A based on graphene-supported TiO_2 mesocrystal. *Sens. Actuators, B* **2016**, *232*, 226−233.
(13) Huo, X.; Liu, P.; Zhu, J.; Liu, X.; Ju, H. Electrochemical immunosensor constructed using TiO2 nanotubes as immobilization scaffold and tracing tag. *Biosens. Bioelectron.* **2016**, *85*, 698−706.
(14) Nallal, M.; Anantha Iyengar, G.; Pill-Lee, K. New Titanium Dioxide-Based Heterojunction Nanohybrid for Highly Selective Photoelectrochemical-Electrochemical Dual-Mode Sensors. *ACS Appl. Mater. Interfaces* **2017**, *9* (42), 37166−37183.
(15) Jampaiah, D.; Srinivasa Reddy, T.; Coyle, V. E.; Nafady, A.; Bhargava, S. K. Co_3O_4@CeO_2 hybrid flower-like microspheres: a strong synergistic peroxidase-mimicking artificial enzyme with high sensitivity for glucose detection. *J. Mater. Chem. B* **2017**, *5* (4), 720−730.
(16) Lopes, J. H.; Colson, F. X.; Barralet, J. E.; Merle, G. Electrically wired enzyme/TiO_2 composite for glucose detection. *Materials science & engineering. C, Materials for biological applications* **2017**, *76*, 991−996.
(17) Cai, G.; Yu, Z.; Ren, R.; Tang, D. Exciton−Plasmon Interaction between AuNPs/Graphene Nanohybrids and CdS Quantum Dots/TiO_2 for Photoelectrochemical Aptasensing of Prostate-Specific Antigen. *ACS sensors* **2018**, *3* (3), 632−639.
(18) Shu, J.; Qiu, Z.; Lv, S.; Zhang, K.; Tang, D. Plasmonic Enhancement Coupling with Defect-Engineered TiO_{2-x}: A Mode for Sensitive Photoelectrochemical Biosensing. *Anal. Chem.* **2018**, *90* (4), 2425−2429.
(19) Qiu, Z.; Shu, J.; Tang, D. Near-Infrared-to-Ultraviolet Light-Mediated Photoelectrochemical Aptasensing Platform for Cancer Biomarker Based on Core−Shell $NaYF_4$:Yb,Tm@TiO_2 Upconversion Microrods. *Anal. Chem.* **2018**, *90* (1), 1021−1028.
(20) Yu, X.; Zhao, Z.; Zhang, J.; Guo, W.; Qiu, J.; Li, D.; Li, Z.; Mou, X.; Li, L.; Li, A.; Liu, H. Rutile Nanorod/Anatase Nanowire Junction Array as Both Sensor and Power Supplier for High-Performance, Self-Powered, Wireless UV Photodetector. *Small* **2016**, *12* (20), 2759−67.
(21) Yan, B.; Zhuang, Y.; Jiang, Y.; Xu, W.; Chen, Y.; Tu, J.; Wang, X.; Wu, Q. Enhanced photoeletrochemical biosensing performance from rutile nanorod/anatase nanowire junction array. *Appl. Surf. Sci.* **2018**, *458*, 382−388.
(22) Cao, F.; Xiong, J.; Wu, F.; Liu, Q.; Shi, Z.; Yu, Y.; Wang, X.; Li, L. Enhanced Photoelectrochemical Performance from Rationally Designed Anatase/Rutile TiO_2 Heterostructures. *Acs Appl. Mater. Inter* **2016**, *8* (19), 12239−12245.
(23) Yu, Z.; Gong, H.; Li, Y.; Xu, J.; Zhang, J.; Zeng, Y.; Liu, X.; Tang, D. Chemiluminescence-Derived Self-Powered Photoelectrochemical Immunoassay for Detecting a Low-Abundance Disease-Related Protein. *Anal. Chem.* **2021**, *93* (39), 13389−13397.
(24) Shu, J.; Tang, D. Recent Advances in Photoelectrochemical Sensing: From Engineered Photoactive Materials to Sensing Devices and Detection Modes. *Anal. Chem.* **2020**, *92* (1), 363−377.
(25) Li, Y.; Lv, K.; Ho, W.; Dong, F.; Wu, X.; Xia, Y. Hybridization of rutile TiO_2 ($rTiO_2$) with g-C_3N_4 quantum dots (CN QDs): An efficient visible-light-driven Z-scheme hybridized photocatalyst. *Applied Catalysis B: Environmental* **2017**, *202*, 611−619.
(26) Gao, C.; Wei, T.; Zhang, Y.; Song, X.; Huan, Y.; Liu, H.; Zhao, M.; Yu, J.; Chen, X. A Photoresponsive Rutile TiO_2 Heterojunction with Enhanced Electron−Hole Separation for High-Performance Hydrogen Evolution. *Advanced materials* **2019**, *31* (8), 1806596.
(27) Zeng, R.; Luo, Z.; Su, L.; Zhang, L.; Tang, D.; Niessner, R.; Knopp, D. Palindromic Molecular Beacon Based Z-Scheme BiOCl-Au-CdS Photoelectrochemical Biodetection. *Anal. Chem.* **2019**, *91* (3), 2447−2454.
(28) Luo, Z.; Qi, Q.; Zhang, L.; Zeng, R.; Su, L.; Tang, D. Branched Polyethylenimine-Modified Upconversion Nanohybrid-Mediated Photoelectrochemical Immunoassay with Synergistic Effect of Dual-Purpose Copper Ions. *Anal. Chem.* **2019**, *91* (6), 4149−4156.
(29) Alshammari, R. H.; Rajesh, U. C.; Morgan, D. G.; Zaleski, J. M. Au-Cu@PANI Alloy Core Shells for Aerobic Fibrin Degradation under Visible Light Exposure. *ACS Applied Bio Materials* **2020**, *3* (11), 7631−7638.
(30) Li, Y.; Chen, W.; Lu, L. Wearable and Biodegradable Sensors for Human Health Monitoring. *ACS Applied Bio Materials* **2021**, *4* (1), 122−139.
(31) Wang, C.-C.; Wei, S.-C.; Luo, S.-C. Recent Advances and Biomedical Applications of Peptide-Integrated Conducting Polymers. *ACS Applied Bio Materials* **2022**. DOI: 10.1021/acsabm.1c01194
(32) Zhu, J.; Huo, X.; Liu, X.; Ju, H. Gold Nanoparticles Deposited Polyaniline-TiO_2 Nanotube for Surface Plasmon Resonance Enhanced Photoelectrochemical Biosensing. *ACS Appl. Mater. Interfaces* **2016**, *8* (1), 341−9.
(33) Yan, B.; Zhao, X.; Chen, D.; Cao, Y.; Lv, C.; Tu, J.; Wang, X.; Wu, Q. Enhanced photoelectrochemical biosensing performance for Au nanoparticle−polyaniline−TiO_2 heterojunction composites. *Rsc Adv.* **2020**, *10* (72), 43985−43993.